Design and System Evaluation of a Dual-Panel Portable PET (DP-PET)

Tianyi Zeng
Shanghai Advanced Research Institute https://orcid.org/0000-0002-5467-062X
Jiaxu Zheng
United Imaging Healthcare
Xinyuan Xia
United Imaging Healthcare
Xin Chen
United Imaging Healthcare
Beien Wang
United Imaging Healthcare
Shuangyue Zhang
United Imaging Healthcare
Adam Chandler
United Imaging Healthcare
Tuoyu Cao
United Imaging Healthcare
Lingzhi Hu (hlingzhi@gmail.com)
United Imaging Healthcare https://orcid.org/0000-0001-5355-3803
Qun Chen
United Imaging Healthcare
Xu Chu
Shanghai Advanced Research Institute

Original research

Keywords: PET/MR, insert, system performance, portable

Posted Date: March 10th, 2021

DOI: https://doi.org/10.21203/rs.3.rs-300103/v1

Design and System Evaluation of a Dual-Panel Portable PET (DP-PET)

Tianyi Zeng[1,2], Jiaxu Zheng[3], Xinyuan Xia[3], Xin Chen[3], Beien Wang[3], Shuangyue Zhang[3], Adam Chandler[4], Tuoyu Cao[3], Lingzhi Hu[3,4,*], Qun Chen[1,3], Xu Chu[1,3]

[1]Shanghai Advanced Research Institute, Chinese Academy of Sciences, Shanghai 201210, China

[2]University of Chinese Academy of Sciences, Beijing 100049, China.

[3]Shanghai United Imaging Healthcare Co., Ltd., Shanghai 201807, China.

[4]United Imaging Healthcare, America, Texas 77054, USA

*Author to whom any correspondence should be addressed.

E-mail: Lingzhi Hu: hlingzhi@gmail.com

ABSTRACT

Background: Integrated whole-body PET/MR technology continues to mature and is now extensively used in clinical setting. However, due to the special design architecture, integrated whole-body PET/MR comes with a few inherent limitations. Firstly, whole-body PET/MR lacks sensitivity and resolution for focused organs. Secondly, boarder clinical access of integrated PET/MR has been significantly restricted due to its prohibitively high cost. The MR-compatible PET insert is a low cost and flexible PET scanner which can be placed within an MRI bore. However, mobility and configurability of all existing MR-compatible PET insert prototypes remain limited.
Methods: An MR-compatible portable PET insert prototype, Dual-panel Portable PET (DP-PET), has been developed for simultaneous PET/MR imaging. Using SiPM, digital readout electronics, novel carbon fiber shielding, phase-change cooling and MRI compatible battery power, DP-PET was designed to achieve high-sensitivity and high-resolution with compatibility with a clinical 3T MRI scanner. A GPU-based reconstruction method with Resolution Modelling (RM) has been developed for the DP-PET reconstruction. We evaluated the system performance on PET resolution, sensitivity, image quality and the PET/MR interference.
Results: Initial results reveal that the DP-PET prototype worked as expected in the MRI bore and caused minimal compromise to the MRI image quality. The PET performance was measured to show a spatial resolution <= 2mm (parallel to the detector panels), maximum sensitivity =3.6% at the center of FOV and energy resolution = 12.43%. MRI pulsing introduces less than 1% variation to the PET performance measurement results.
Conclusions: We developed a MR-compatible PET insert prototype and performed several studies to begin to characterize the performance of the proposed DP-PET.The results showed that the proposed DP-PET performed well in the MRI bore and would cause little influence on the MRI images. The Derenzo phantom test showed that the

proposed reconstruction method could obtained high quality images using DP-PET.
Key words: PET/MR; insert; system performance; portable

1. Background

Positron Emission Tomography (PET) is a biomedical imaging modality which can provide 3D molecular and functional images by detecting high energy photons generated by the positron and electron annihilation [1-3]. Thanks to the high sensitivity and exquisite specificity of targeted radioactive tracer, PET has been widely used in clinical settings for diagnosis of cancer, neurodegenerative disease and cardiovascular disease [4]. PET is usually performed in combination with other imaging modalities which can offer anatomical structures for localization. Currently there are two types of commercially available hybrid PET systems including PET/CT (X-ray Computed Tomography) and integrated PET/MR (Magnetic Resonance). Although integrated PET/MR is being clinically adopted at a slower pace compared to PET/CT, it is demonstrated as a powerful multimodality imaging tool in medical research and in clinical practice [5]. Compared with CT, MRI features unique advantages in revealing anatomical morphology and physiological function information with superior soft tissue contrast. Furthermore, since there is no ionizing radiation in MRI, it leads to lower radiation dose for pediatric patients and other radiation sensitive patient groups. These features make PET/MR a preferred choice compared with PET/CT in certain clinical applications such as brain imaging, cardiac imaging, and breast imaging.

The integration of PET and MRI is technically challenging, mainly because of the mutual interference between the two subsystems [6]. The major hardware challenges are the electromagnetic compatibility of PET detectors in a strong magnetic field environment, radio frequency interference with magnetic resonance, gradient pulse induced eddy current and additional field inhomogeneity of the main magnetic field introduced by ferromagnetic PET components [7-10]. The image reconstruction for PET/MR also faces unique challenges compared to PET/CT, including MR based attenuation correction [11], truncation compensation [12], and MR based motion correction [13].

The continuing effort to integrate PET and MRI began in the 1990s. In 1997, Shao et al. placed scintillation crystals in a 0.2T MR imaging system [14], and connected them to photomultiplier tubes (PMTs), the light sensors, located outside of the MR magnetic field by means of a long optical fiber to conduct PET/MR imaging research on phantoms. Because Avalanche Photodiode (APD) technology is not sensitive to magnetic fields and can be coupled to scintillation crystals directly or through a very short optical fiber, PET/MR systems based on APD were used to study small animals and human brains at the beginning of the 21st century [15]. Siemens were the first to develop a commercial APD-based PET/MR that could be used for whole body scanning in 2011 [16]. Because APD suffers from slow response to optical signal, it is impossible to measure Time-of-Flight (TOF) based on APD detectors. The recent development of SiPM (Silicon Photomultiplier) technology on the other hand allows faster timing measurements while maintaining sufficient MR compatibility. Both GE Healthcare and

United Imaging Healthcare have developed clinical integrated TOF PET/MR systems using SiPM technology [17, 18].

Integrated whole-body PET/MR technology continues to mature and is now extensively used in clinical setting. However, due to the special design architecture, integrated whole-body PET/MR comes with a few inherent limitations. Firstly, whole-body PET/MR lacks sensitivity and resolution for focused organs, e.g. brain and breast, which limits its further clinical application such as image guided biopsy, T-staging et al. Secondly, boarder clinical access of integrated PET/MR has been significantly restricted due to its prohibitively high cost [19]. The MR-compatible PET insert, on the other hand, is a low cost and flexible PET scanner which can be placed within an MRI bore. MR-compatible PET inserts have been designed to work properly in the presence of a strong magnetic field and require no hardware modification to the MRI system. There have been a few initiatives to develop MR-compatible PET inserts [20-22], which show great potential for their future clinical adoption. A few successful prototypes have been developed for dedicated brain and small animals imaging applications using radiofrequency (RF)-shielding techniques and RF-penetrable technology [23-25]. However, all existing MR-compatible PET insert prototypes require cumbersome power supply systems and cooling systems, and hence mobility and configurability of these systems remain limited.

With the intention to further enhance flexibility and sensitivity while reducing system complexity, we developed a novel portable MR-compatible PET insert, which features novel carbon fiber shielding, battery power supplies, and a phase-change cooling system. We verified its performance in a dual panel configuration - the DP-PET (Dual-panel Portable PET), ideal for breast imaging. A GPU-based reconstruction method with resolution modelling was developed for the DP-PET reconstruction. In this paper, we present the system design, reconstruction, and characterization of the prototype MR-compatible DP-PET. PET performance as well as the mutual interaction between PET and MRI were also investigated.

2. Methods

2.1. System Design and Specification

The MRI compatible and portable PET insert, DP-PET, consists of two panel detector modules each encased in carbon fiber Faraday cage. We define the system coordinate as:x: vertical direction of DP-PET; y: MRI axial direction; z: the direction perpendicular to the two parallel detector panels.

Each detector module contains 5×7 blocks with 7 blocks along the y direction, while each block has 4 SiPM detector readouts coupled to an array of 7×8 15.5×2.76×2.76 mm^3 LYSO crystals. The internal light guide of the crystals is a proprietary design, and the modules were manufactured by United Imaging Healthcare Co., Ltd. (UIH), Shanghai. The entire DP-PET system has 3,920 crystals, with each panel containing 35 crystals in the x direction and 56 crystals in y direction. The total dimension of each panel is 370 mm (y) by 110 mm (x). The panel spacing is variable, but for this study we set it to 160 mm as this is the typical width of a pendant breast. The dimension of the FOV is 100×160×160 mm^3, with the central FOV offset defined

as (0, 0, 0) mm.

Figure 1 shows the mechanical structure for one of the detector modules from the DP-PET insert. Data from the SiPMs are read out and pre-processed by a Field Programmable Gate Array (FPGA) on the FPGA board, which also contains an optical transceiver synchronized with the opposite detector module (through an optical fiber). The pre-processed data is formatted and transmitted via a high-speed optical fiber to a post-processing board mounted via a PCIe interface on the control PC at a 1.5 Gbps data rate. The *Single event* data is then converted to *Coincidence event* data through an offline coincidence sorting module, with a 4ns timing window and a 430-600 keV energy window. The FPGA board is powered by a set of 2 MR-compatible battery packs in series (6000 mAh) and the 30V bias voltage of the SiPM board is powered by a set of 8-battery packs in series (24000 mAh). With the power of the whole system being 10W, DP-PET can operate for 60 minutes with fully charged battery packs.

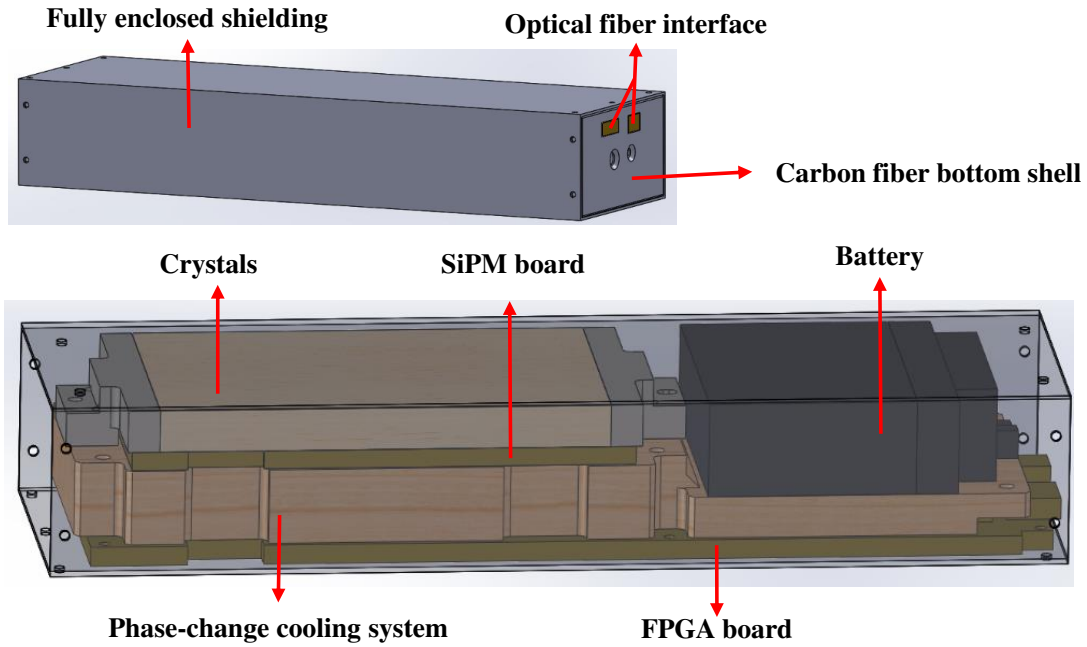

Figure 1: Mechanical structure of one detector module

The mechanical support and shielding structure of the DP-PET is designed to effectively shield electromagnetic waves from the MRI system. In order to eliminate the eddy current generated by the shielding shell, we used carbon fiber shielding to replace the traditional metal shielding. In addition, soft conductive materials were contained at the joints to increase sealing performance. Since there is no large areas or large metal in the whole DP-PET scanner, it presents good electromagnetic compatibility with the MRI system. Figure 2 shows the prototype DP-PET system mounted on the patient bed of a clinical 3T MRI system (uMR790, UIH, Shanghai).

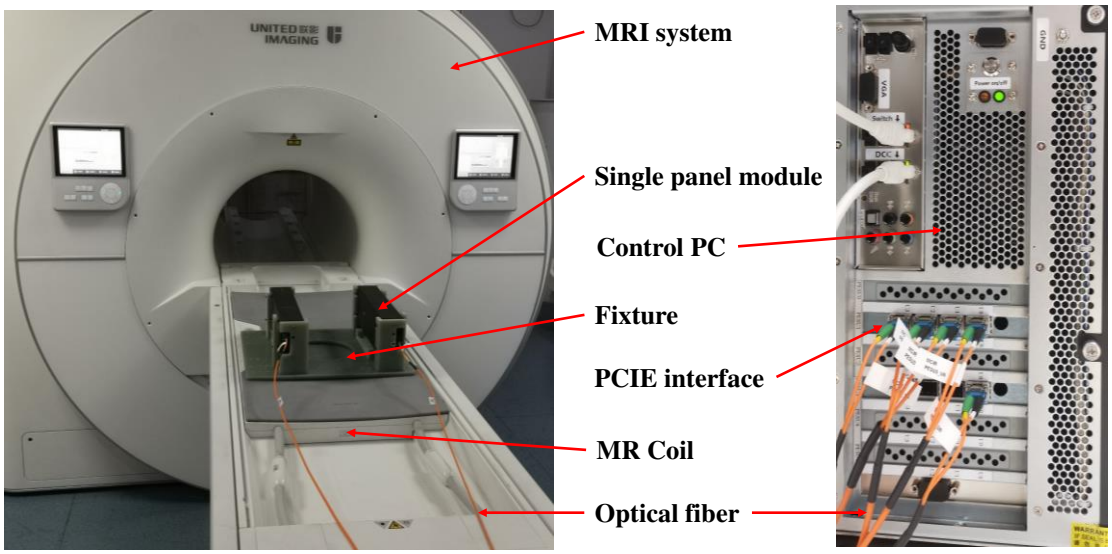

Figure 2: Picture of DP-PET inserted MR system

Considering the flexibility and portability, the water-cooling system which is commonly used in commercial PET scanners was replaced by a phase-change cooling system in the DP-PET. Figure 3 shows the schematic of the phase-change cooling system. The phase-change cooling system is composed of phase-change cooling material and thermal silica. This material absorbs large amount of heat when the rising-temperature caused by phase-changes occur so it can maintain the temperature near the phase-change point [26, 27]. The cooling system was attached to SiPM board, FPGA board and batteries which are prone to generate heat during operation. After connecting with the cold source, it can quickly release heat through thermal silica and be reused.

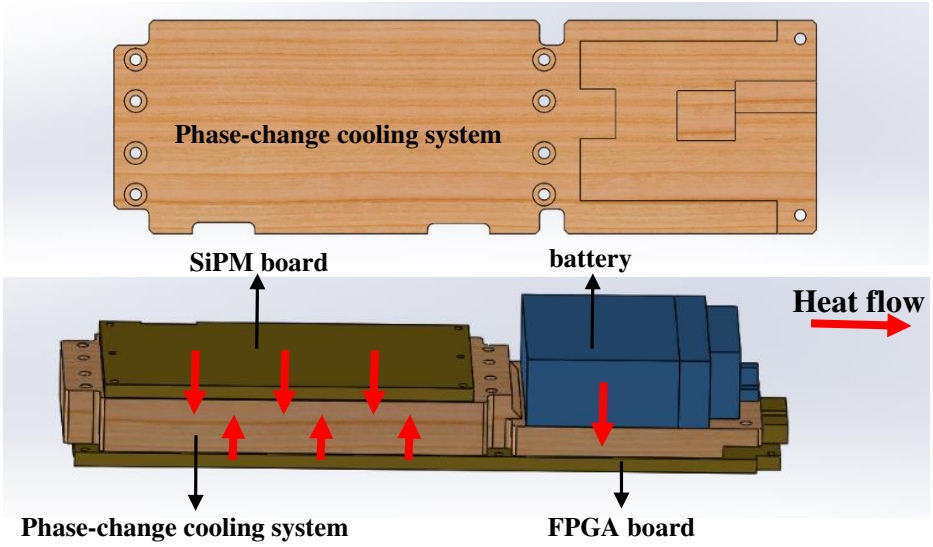

Figure 3: Schematic of phase-change cooling system

Before reconstruction, the list-mode data was firstly transferred to panelgram (sinogram of dual-panel systems) data. The crystal IDs of the coincidence crystal pair were read from list-mode data and were counted in panelgram. A GPU-accelerated iterative image reconstruction method was developed based on the MLEM (Maximum likelihood expectation maximization) algorithm and PSF (Point spread function)

resolution modelling [28]. The GPU kernel function was implemented to compute the forward projection and back projection in the Line-of-response (LOR) units. The normalization correction matrix was acquired by scanning a plane source of 155×90×5 mm^3 filled with ^{18}F-FDG and placed parallel to the two detector panels. The normalization correction matrix was first back projected to precompute a sensitivity map. Some modifications were applied to the reconstruction method in order to better fit the DP-PET. A tube-of-response (TOR) based ray-tracing algorithm, in which the sum of cross sections between the voxels, dubbed TOR, instead of the line integrals of LORs was calculated [29] replacing the Siddon ray-tracing method which has been widely used in clincial PET reconstruction [30]. Random, attenuation and scatter corrections were included in the reconstruction code. The random events of every measurement were estimated by the delayed coincidence method with a delay offset of 500ns [31]. The attenuation maps were segmented from 3D MRI images (3D Dixon in-phase/out-phase Imaging sequence). Scatter correction was based on single scatter simulation with L1-norm tail fitting [32]. All the corrections were performed in the GPU using parallel computing within several seconds. Point source measurements were performed to obtain the PSFs for resolution modelling (RM) during reconstructions. A Gaussian mixture model was used for RM to accurately capture the asymmetric PSF shapes in the reconstructed images [33]. The RM was spatially variant and was applied in the reconstruction program by a PSF operation before projection as well as a transposed PSF operation after back projection. Including RM in the reconstruction increased the calculation time by approximately 10%. The scale of the output reconstructed image was 140×224×160, with a voxel size of 0.713×0.713×1.0 mm^3.

2.2. Measurements

To evaluate the spatial resolution of DP-PET, a ^{22}Na point source with 110 kBq activity was scanned at 18 separate positions (8 minutes per position), including x offsets of (0, 20, 40) mm, y offsets of (0, 20, 40) mm and z offsets of (0, 40) mm in the field of view (FOV). MRI was idle during the whole scans and the scans were repeated 3 independent times. Due to the lack of complete angel information, the filtered back projection algorithm suggested by NEMA could not be performed [34]. We instead used the proposed iterative reconstruction method (without RM) to reconstruct the point source images, and the full width at half maximum (FWHM) were determined by a Gaussian fitting. The number of iterations for the reconstruction was 20.

For sensitivity measurement, ^{22}Na source was scanned at y offsets of (0, 10, 20, 30, 40) mm and z offsets of (0, 10, 20, 30, 40) mm (30 seconds per position). MRI was idle during the whole scan and the scans were repeated 3 independent times. The random event rate was less than 5% of the true event rate. The background count rate was recorded as R_b, and the count rate of ith point source measurement was recorded as R_i. The absolute sensitivity was calculated as:

$$S_i = \frac{(R_i - R_b)}{\gamma A}, \quad (1)$$

where γ is the branching ratio of ^{22}Na, and A is the activity of the source.

For energy resolution measurement, a^{68}Ge line source with 11.4 MBq activity was

scanned for 10 minutes. The source was positioned along the z axis of DP-PET and was positioned at the center of the FOV. The scans were repeated 3 independent times. *Single events* were recorded to calculate energy resolution. Gaussian fitting was used for the energy spectrum of every crystal, and the result was the average energy resolution of all crystals.

We evaluate the interference between DP-PET and MRI from two different perspectives: the influence of the DP-PET insert on the MRI and the influence of the MRI on the DP-PET. To analyze the influence of the DP-PET on the MRI, an 8×7×12 cm^3 cuboid phantom (water, $NiSO_4$, NaCl) was imaged using a 3D Dixon in-phase/out-phase sequence (TR / TE = 4.91 / 3.19 ms, voxel size= 0.91×0.91×2 mm^3, 549×384×164 voxels, pixel bandwith = 1080 Hz, 39s measurement time) with and without the DP-PET in the MR bore. The Signal-to-Noise Ratio (SNR) and image uniformity were assessed for the MR images acquired with and without the DP-PET in the MRI bore to determine if there was any interference caused by the DP-PET on the image quality. To analyze the influence of the MRI on the DP-PET, ^{22}Na point source was scanned at the center of the FOV (source position (0,0,0)mm) and the spatial resolution and sensitivity was calculated while the MRI was pulsing (3D Dixon in-phase/out-phase sequence, 8 minutes measurement time) and these were compared with results obtained when the MRI was idle. The number of iterations for the reconstruction was 20. The experiments were repeated for 3 times.

To assess the spatial resolution of the DP-PET system at clinically realistic activity concentration level, a Derenzo resolution phantom [35] (3D printed with transparent photosensitive resin; shown in Figure 4) filled with 444 kBq/mL (in total 11.1 Mbq) ^{18}F-FDG was scanned. To evaluate the PET image quality, a PET scan was performed with the axis of the cylindrical phantom parallel to the z direction.

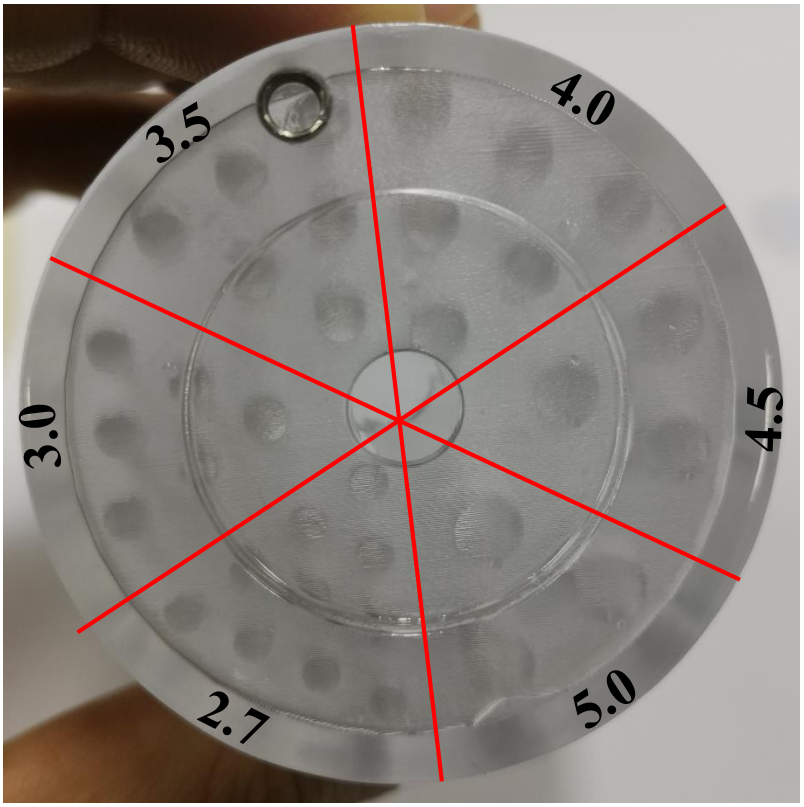

Figure 4: The Derenzo resolution phantom with rod diameters (in mm) indicated

3. Results

3.1. Spatial Resolution

The FWHM spatial resolution values are summarized in Table I. The spatial resolution (average ± the standard deviation) from three independent measurements in the x, y and z directions are shown. The spatial resolutions at the center of the FOV (source position (0,0,0)mm) were 1.66 mm, 1.72 mm, and 6.04 mm in x, y and z directions respectively. The reduced resolution in the z direction resolution is because of the limited angular coverage due to the limited size of detector panels. The spatial resolution in the z direction was uniform with z = 0 mm. However, when there was an offset in the z direction (40 mm in this example), the reduction in the spatial resolution in the z direction becomes more significant.

Table I: Point source spatial resolution at different positions

Source Position (x, y, z) mm	Spatial Resolution (mm)		
	x	y	z
（0, 0, 0）	1.66 ± 0.04	1.72 ± 0.05	6.04 ± 0.19
（0, 20, 0）	1.64 ± 0.05	1.71 ± 0.05	5.98 ± 0.19
（0, 40, 0）	1.64 ± 0.02	1.60 ± 0.02	6.13 ± 0.21
（20, 0, 0）	1.59 ± 0.04	1.78 ± 0.10	6.04 ± 0.23
（20, 20, 0）	1.43 ± 0.10	1.71 ± 0.07	5.84 ± 0.18
（20, 40, 0）	1.38 ± 0.08	1.67 ± 0.05	6.15 ± 0.23
（40, 0, 0）	1.23 ± 0.03	1.59 ± 0.10	5.71 ± 0.21
（40, 20, 0）	1.27 ± 0.03	1.66 ± 0.05	5.97 ± 0.17
（40, 40, 0）	1.30 ± 0.04	1.25 ± 0.08	6.20 ± 0.30
（0, 0, 40）	1.49 ± 0.03	1.62 ± 0.04	7.10 ± 0.28
（0, 20, 40）	1.47 ± 0.05	1.65 ± 0.02	6.97 ± 0.23
（0, 40, 40）	1.45 ± 0.05	1.68 ± 0.04	7.24 ± 0.32
（20, 0, 40）	1.55 ± 0.04	1.62 ± 0.03	6.88 ± 0.26
（20, 20, 40）	1.53 ± 0.05	1.61 ± 0.04	6.93 ± 0.30
（20, 40, 40）	1.54 ± 0.04	1.64 ± 0.04	7.31 ± 0.29
（40, 0, 40）	1.28 ± 0.02	1.66 ± 0.03	6.58 ± 0.22
（40, 20, 40）	1.20 ± 0.02	1.61 ± 0.02	6.98 ± 0.23
（40, 40, 40）	1.45 ± 0.04	1.57 ± 0.04	7.56 ± 0.25

3.2. Sensitivity

Table II shows the sensitivity % (average ± standard deviations) from three independent measurements for different positions of the point source. The sensitivity at the center of FOV (source position (0,0,0)mm) is 3.59%. Whether along y axis or z axis, moving away from the center of FOV decreases the sensitivity of DP-PET. But, at the edge of the FOV (40mm offset), DP-PET maintains relatively high sensitivity of no less than 2.27%.

Table II: Sensitivity at different positions

Source Position (x, y, z) mm	Sensitivity
（0, 0, 0）	3.59% ± 0.03%
（0, 10, 0）	3.36% ± 0.02%
（0, 20, 0）	3.01% ± 0.01%
（0, 30, 0）	2.73% ± 0.01%
（0, 40, 0）	2.27% ± 0.01%
（0, 0, 10）	3.28% ± 0.02%
（0, 0, 20）	2.84% ± 0.02%
（0, 0, 30）	2.52% ± 0.03%
（0, 0, 40）	2.30% ± 0.01%

3.3. Energy Resolution

The average energy resolution % for DP-PET was calculated by taking the average of every individual crystal's energy resolution. The results are averaged from three independent measurements. Figure 5 shows the histogram of the energy resolution for all individual crystals. The energy resolution of 94% crystals is between 12% and 13%. The average system energy resolution was measured to be 12.43%±0.04%.

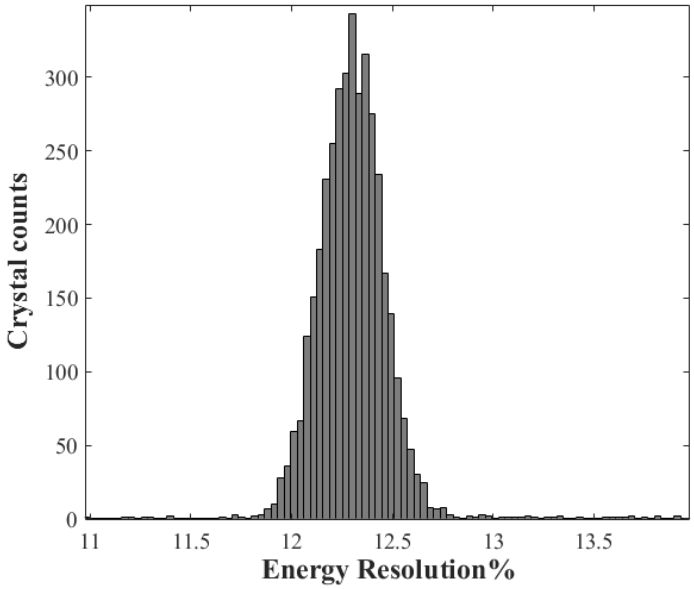

Figure 5: Energy resolution histogram of individual crystals

3.4. PET/MR Interference

Figure 6 shows the MRI images obtained under two different conditions (no DP-PET and DP-PET inserted) and the resulting image from subtracting them. No visible artifacts were found in the images when the DP-PET was inserted into the MRI bore. The subtraction image shows that the edges of the image suffered the most when DP-PET was inserted. In order to quantify the differences between no DP-PET and DP-PET inserted, MRI images were firstly segmented and a 3D region of interest (ROI) with at least 75 percent of the phantom volume was covered (Fig. 6(a)). The SNR within the ROI was calculated by dividing the mean value of the ROI by the standard deviation of the ROI. The MR image uniformity was accessed by using the method of Normalized

Absolute Average Deviation Uniformity described in the NEMA standards publication MS 3-2008 [36]. The results, shown in Table III, were from three independent measurements with the average values and standard deviations displayed. Relative to no DP-PET inserted, when DP-PET was inserted, the mean SNR decreased by 3.88% and 1.75% for Dixon in-phase and Dixon out-phase, respectively. The image uniformity also decreased 1.01% for Dixon in-phase and 0.88% compared to when no DP-PET was present. These results suggest that putting the DP-PET in the MRI bore does not dramatically interfere with the MRI.

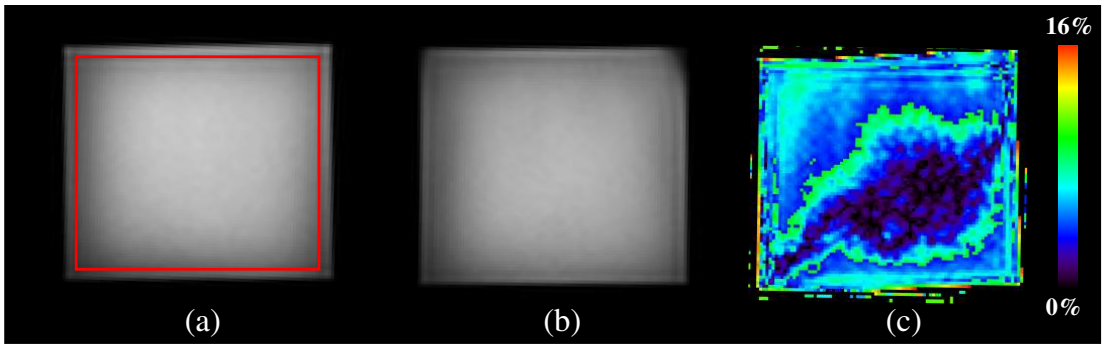

Figure 6: Dixon MR images with no DP-PET (a) and DP-PET inserted (b), and (c) is the result of subtracting (a) and (b)

Table III: SNR and Image Uniformity under different conditions

Conditions	SNR	Image Uniformity
No DP-PET with Dixon in-phase	5.04 ± 0.00	83.74% ± 0.04%
DP-PET inserted with Dixon in-phase	4.85 ± 0.02	82.90% ± 0.05%
No DP-PET with Dixon out-phase	4.79 ± 0.01	83.12% ± 0.03%
DP-PET inserted with Dixon out-phase	4.70 ± 0.04	82.38% ± 0.13%

To evaluate the influence of the MRI pulsing on the PET performance, Table IV shows the spatial resolution and sensitivity while the MRI was pulsing, relative to when the MRI was idle. The spatial resolution of the point source is reduced by3% and the sensitivity has a decrease below 1% under MRI pulsing. There is in general less than 5% difference in spatial resolution and sensitivity with or without MRI pulsing, demonstrating that DP-PET can work properly under MRI pulsing.

Table IV: Spatial Resolution and Sensitivity under different conditions

PET performance	MR idle	MR pulsing
Spatial Resolution (x, y, z) mm	1.66 ± 0.04	1.71 ± 0.08
	1.72 ± 0.05	1.75 ± 0.01
	6.04 ± 0.19	6.05 ± 0.21
Sensitivity	3.59% ± 0.03%	3.58% ± 0.02%

3.5. PET Imaging of the Spatial Resolution Phantom

Figure 7 shows images of the Derenzo phantom scanned parallel to the z directions with RM off and on. Images were reconstructed with all corrections. The number of iterations for scatter correction was 3, and the number of iterations for reconstruction was 100. All six segments are visible and the smallest rods of 2.7 mm can be perfectly determined with high contrast. This demonstrates that the high spatial resolution of the x and y direction.

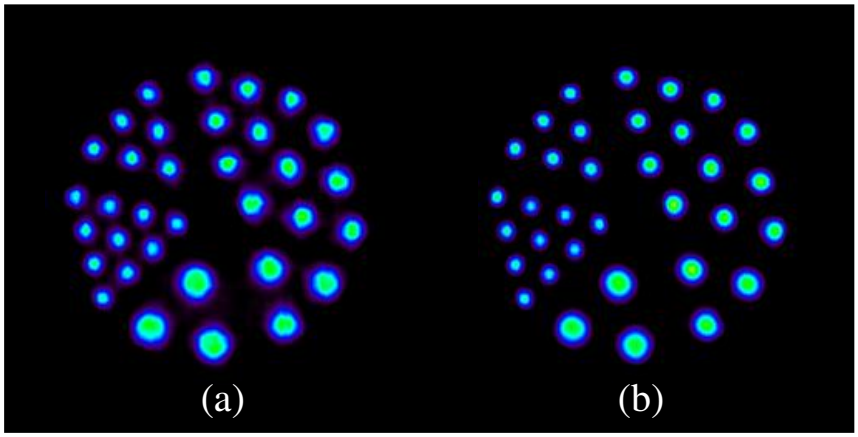

Figure 7: Images of the Derenzo phantom scanned parallel to the z direction with RM off (a) and RM on (b) from DP-PET scan

4. Discussion and Conclusion

In this work, we developed a portable MR-compatible PET insert and evaluated its performance inside a clinical 3T MRI scanner. Measurement results of the DP-PET demonstrated high resolution and sensitivity during simultaneous PET/MR acquisition. Because of its unique battery power pack and cable-less cooling design, the DP-PET can potentially be used for a large variety of clinical and research applications. For instance, without additional hardware modification, a clinical MRI scanner can achieve simultaneous PET/MR imaging for targeted organs such as brain and breast.

In addition, compared to integrated PET/MR, which is often priced as high as $4 million USD, the DP-PET inserted in a clinical MRI will be an economical alternative with excellent performance to cost balance. The DP-PET prototype cost only one-tenth of a whole-body PET/MR system, and it can work in almost every radiation shielded space. Therefore, low-cost DP-PET is potentially useful for promoting more accessible multi-modal PET/MR technology and exploring more clinical research applications.

We chose dual-panel breast imaging as the first configuration for verification of DP-PET. Mammography and ultrasound are the most common methods for diagnosis and guided intervention in breast disease. MRI has also become an increasingly important method in breast cancer diagnosis and post-operation examination [37]. Breast-dedicated PET imaging systems have been developed in recent years and demonstrate the clinical feasibility [38-40]. The dual-panel geometry in breast-dedicated PET has been widely used due to the advantage of lower costs and potentially increased sensitivity [41-43]. There is a growing interest in developing breast PET/MR,

and some simulation studies as well as prototypes have proved the increased sensitivity and specificity in detection of small lesions [44, 45]. In considering biopsy applications in breast, a dual-panel detector configuration is more practical than a ring detector for the convenience of breast immobilization [46]. Our study demonstrated that the proposed DP-PET insert prototype maintained high performance inside a strong magnetic field which shows great promise for breast PET/MR applications.

There are a few limitations in this study. Because there isn't a matching MRI breast coil, all images were collected using whole body transmit/receive coil which might achieve sub-optimal MRI image quality. We are still working on developing a dedicated breast coil for DP-PET. An ideally designed breast coil should not affect the uniformity of the main magnetic field, and the coil should be designed to be gamma transparent [47]. When considering the flexibility of the DP-PET, the coil should allow for variable spacing and be exchangeable. Moreover, the proposed DP-PET was a prototype system, and therefore there was limited testing of the battery power supply robustness and limitations of the phase-change cooling material.

In conclusion, we developed a MR-compatible PET insert prototype and performed several studies to begin to characterize the performance of the proposed DP-PET and presented the initial results here. Measurements of PET performance demonstrate that DP-PET has a spatial resolution better than 2 mm (parallel to the detector panels) and a maximum sensitivity of 3.59% in the center of FOV. In addition, the energy resolution was measured to be an average of 12.43%. We also studied the interference between DP-PET and 3T MRI system. The results showed that the proposed DP-PET could work optimally in the MRI bore and would cause little influence on the MRI images. Finally, a Derenzo phantom was scanned in DP-PET. With all corrections and RM applied, high quality images were obtained using the proposed GPU-based reconstruction method.

Acknowledgements

The authors would like to acknowledge and thank Yang Xu for design FPGA logic in DP-PET system.

Authors' contributions

Tuoyu Cao, Lingzhi Hu, Xinyuan Xia and Jiaxu Zheng designed the DP-PET hardware system. Xin Chen and Beien Wang helped complete the measurements. Tianyi Zeng developed the reconstruction program, analyzed the data, and wrote the manuscript draft The authors read, critically reviewed, and approved the final manuscript.

Funding

The authors received funding for the work associated with this paper from China's Ministry of science and technology "digital medical equipment research and development" No.2016YFC0103900.

Availability of data and materials

The datasets used and analyzed during the current study are available form the corresponding author on reasonable request.

Declarations

Ethics approval and consent to participate

Not applicable

Consent for publication

Not applicable

Competing interests

This study was performed as part of the first author's PhD project. The other authors declare that they have no competing interests.

References

1. Zeng T, Yang H, Cao T, Hu L, Chu X, Lu X, et al. [Timing calibration comparison research of integrated TOF-PET/MR]. Sheng Wu Yi Xue Gong Cheng Xue Za Zhi. 2019;36:1003-11. doi:10.7507/1001-5515.201809044.
2. Torres Espallardo I. PET/CT: underlying physics, instrumentation, and advances. Radiologia. 2017;59:431-45. doi:10.1016/j.rx.2016.10.010.
3. Hu Z, Li Y, Zou S, Xue H, Sang Z, Liu X, et al. Obtaining PET/CT images from non-attenuation corrected PET images in a single PET system using Wasserstein generative adversarial networks. Phys Med Biol. 2020;65:215010. doi:10.1088/1361-6560/aba5e9.
4. Hess S, Blomberg BA, Zhu HJ, Hoilund-Carlsen PF, Alavi A. The pivotal role of FDG-PET/CT in modern medicine. Acad Radiol. 2014;21:232-49. doi:10.1016/j.acra.2013.11.002.
5. Bailey D, Pichler B, Gückel B, Barthel H, Beer A, Bremerich J, et al. Combined PET/MRI: multi-modality multi-parametric imaging is here. Molecular imaging and biology. 2015;17:595-608.
6. Vaska P, Cao T. The state of instrumentation for combined positron emission tomography and magnetic resonance imaging. Semin Nucl Med. 2013;43:11-8. doi:10.1053/j.semnuclmed.2012.08.003.
7. Kong HJ, Kim TH, Jo SE, Oh MS. Smart three-dimensional imaging LADAR using two Geiger-mode avalanche photodiodes. Opt Express. 2011;19:19323-9. doi:10.1364/OE.19.019323.
8. Roncali E, Cherry SR. Application of silicon photomultipliers to positron emission tomography. Ann Biomed Eng. 2011;39:1358-77. doi:10.1007/s10439-011-0266-9.
9. Delso G, Ziegler S. PET/MRI system design. Eur J Nucl Med Mol Imaging. 2009;36 Suppl 1:S86-92. doi:10.1007/s00259-008-1008-6.
10. Peng BJ, Walton JH, Cherry SR, Willig-Onwuachi J. Studies of the interactions of an MRI system with the shielding in a combined PET/MRI scanner. Phys Med Biol. 2010;55:265-80. doi:10.1088/0031-9155/55/1/016.
11. Keller SH, Holm S, Hansen AE, Sattler B, Andersen F, Klausen TL, et al. Image artifacts from MR-based attenuation correction in clinical, whole-body PET/MRI. MAGMA. 2013;26:173-81. doi:10.1007/s10334-012-0345-4.
12. Schramm G, Langner J, Hofheinz F, Petr J, Lougovski A, Beuthien-Baumann B, et al. Influence and compensation of truncation artifacts in MR-based attenuation correction in PET/MR. IEEE Trans Med Imaging. 2013;32:2056-63. doi:10.1109/TMI.2013.2272660.

13. Petibon Y, Sun T, Han PK, Ma C, Fakhri GE, Ouyang J. MR-based cardiac and respiratory motion correction of PET: application to static and dynamic cardiac (18)F-FDG imaging. Phys Med Biol. 2019;64:195009. doi:10.1088/1361-6560/ab39c2.
14. Shao Y, Cherry SR, Farahani K, Meadors K, Siegel S, Silverman RW, et al. Simultaneous PET and MR imaging. Phys Med Biol. 1997;42:1965-70. doi:10.1088/0031-9155/42/10/010.
15. Judenhofer MS, Wehrl HF, Newport DF, Catana C, Siegel SB, Becker M, et al. Simultaneous PET-MRI: a new approach for functional and morphological imaging. Nat Med. 2008;14:459-65. doi:10.1038/nm1700.
16. Pichler BJ, Wehrl HF, Judenhofer MS. Latest advances in molecular imaging instrumentation. J Nucl Med. 2008;49 Suppl 2:5S-23S. doi:10.2967/jnumed.108.045880.
17. Grant AM, Deller TW, Khalighi MM, Maramraju SH, Delso G, Levin CS. NEMA NU 2-2012 performance studies for the SiPM-based ToF-PET component of the GE SIGNA PET/MR system. Med Phys. 2016;43:2334. doi:10.1118/1.4945416.
18. Chen S, Gu Y, Yu H, Chen X, Cao T, Hu L, et al. NEMA NU2-2012 performance measurements of the United Imaging uPMR790: an integrated PET/MR system. Eur J Nucl Med Mol Imaging. 2021. doi:10.1007/s00259-020-05135-9.
19. Lee BJ, Grant AM, Chang CM, Watkins RD, Glover GH, Levin CS. MR Performance in the Presence of a Radio Frequency-Penetrable Positron Emission Tomography (PET) Insert for Simultaneous PET/MRI. IEEE Trans Med Imaging. 2018;37:2060-9. doi:10.1109/TMI.2018.2815620.
20. Hallen P, Schug D, Wehner J, Weissler B, Gebhardt P, Goldschmidt B, et al. Evaluation of PET performance and MR compatibility of a preclinical PET/MR insert with digital silicon photomultiplier technology. EJNMMI Phys. 2015;2:A55. doi:10.1186/2197-7364-2-S1-A55.
21. Hallen P, Schug D, Weissler B, Gebhardt P, Salomon A, Kiessling F, et al. PET performance evaluation of the small-animal Hyperion II(D) PET/MRI insert based on the NEMA NU-4 standard. Biomed Phys Eng Express. 2018;4:065027. doi:10.1088/2057-1976/aae6c2.
22. Schug D, Wehner J, Dueppenbecker PM, Weissler B, Gebhardt P, Goldschmidt B, et al. ToF performance evaluation of a PET insert with Digital Silicon Photomultiplier technology during MR operation. EJNMMI Phys. 2014;1:A20. doi:10.1186/2197-7364-1-S1-A20.
23. Grant AM, Lee BJ, Chang CM, Levin CS. Simultaneous PET/MR imaging with a radio frequency-penetrable PET insert. Med Phys. 2017;44:112-20. doi:10.1002/mp.12031.
24. Kuang Z, Wang X, Ren N, Wu S, Gao J, Zeng T, et al. Design and performance of SIAT aPET: a uniform high-resolution small animal PET scanner using dual-ended readout detectors. Phys Med Biol. 2020;65:235013. doi:10.1088/1361-6560/abbc83.
25. Stortz G, Thiessen JD, Bishop D, Khan MS, Kozlowski P, Retiere F, et al. Performance of a PET Insert for High-Resolution Small-Animal PET/MRI at 7 Tesla. J Nucl Med. 2018;59:536-42. doi:10.2967/jnumed.116.187666.
26. Jiang Z, Yang W, He F, Xie C, Fan J, Wu J, et al. Microencapsulated Paraffin Phase-Change Material with Calcium Carbonate Shell for Thermal Energy Storage and Solar-Thermal Conversion. Langmuir. 2018;34:14254-64. doi:10.1021/acs.langmuir.8b03084.
27. Jianyu Z, Yongjie Y, Lugang B, Jinsheng G, Zhonghe Z, Jinliang P, et al. Development of a new type of low-temperature pattern wax. Petroleum science and technology. 2001;19:1119-28.
28. Zeng T, Gao J, Gao D, Kuang Z, Sang Z, Wang X, et al. A GPU-accelerated fully 3D OSEM image reconstruction for a high-resolution small animal PET scanner using dual-ended readout detectors. Phys Med Biol. 2020;65:245007. doi:10.1088/1361-6560/aba6f9.

29. Gu X-Y, Zhou W, Li L, Wei L, Yin P-F, Shang L-M, et al. High resolution image reconstruction method for a double-plane PET system with changeable spacing. Chinese physics C. 2016;40:058201.
30. Siddon RL. Prism representation: a 3D ray-tracing algorithm for radiotherapy applications. Phys Med Biol. 1985;30:817-24. doi:10.1088/0031-9155/30/8/005.
31. Brasse D, Kinahan PE, Lartizien C, Comtat C, Casey M, Michel C. Correction methods for random coincidences in fully 3D whole-body PET: impact on data and image quality. J Nucl Med. 2005;46:859-67.
32. Werling A, Bublitz O, Doll J, Adam LE, Brix G. Fast implementation of the single scatter simulation algorithm and its use in iterative image reconstruction of PET data. Phys Med Biol. 2002;47:2947-60. doi:10.1088/0031-9155/47/16/310.
33. Matej S, Li Y, Panetta J, Karp JS, Surti S. Image-based Modeling of PSF Deformation with Application to Limited Angle PET Data. IEEE Trans Nucl Sci. 2016;63:2599-606. doi:10.1109/TNS.2016.2607019.
34. Goertzen AL, Bao Q, Bergeron M, Blankemeyer E, Blinder S, Canadas M, et al. NEMA NU 4-2008 comparison of preclinical PET imaging systems. J Nucl Med. 2012;53:1300-9. doi:10.2967/jnumed.111.099382.
35. Wang B, van Roosmalen J, Kreuger R, Huizenga J, Beekman FJ, Goorden MC. Characterization of a multi-pinhole molecular breast tomosynthesis scanner. Phys Med Biol. 2020;65:195010. doi:10.1088/1361-6560/ab9eff.
36. Blinov NN, Snopova KA. [Problems of certification and quality monitoring of magnetic resonance imaging rooms]. Med Tekh. 2014:34-7.
37. Alcantara D, Leal MP, Garcia-Bocanegra I, Garcia-Martin ML. Molecular imaging of breast cancer: present and future directions. Front Chem. 2014;2:112. doi:10.3389/fchem.2014.00112.
38. Koolen BB, Vogel WV, Vrancken Peeters MJ, Loo CE, Rutgers EJ, Valdes Olmos RA. Molecular Imaging in Breast Cancer: From Whole-Body PET/CT to Dedicated Breast PET. J Oncol. 2012;2012:438647. doi:10.1155/2012/438647.
39. Raylman RR, Abraham J, Hazard H, Koren C, Filburn S, Schreiman JS, et al. Initial clinical test of a breast-PET scanner. J Med Imaging Radiat Oncol. 2011;55:58-64. doi:10.1111/j.1754-9485.2010.02230.x.
40. Iima M, Nakamoto Y, Kanao S, Sugie T, Ueno T, Kawada M, et al. Clinical performance of 2 dedicated PET scanners for breast imaging: initial evaluation. J Nucl Med. 2012;53:1534-42. doi:10.2967/jnumed.111.100958.
41. Zhang J, Olcott PD, Chinn G, Foudray AM, Levine CS. Study of the performance of a novel 1 mm resolution dual-panel PET camera design dedicated to breast cancer imaging using Monte Carlo simulation. Med Phys. 2007;34:689-702. doi:10.1118/1.2409480.
42. MacDonald L, Edwards J, Lewellen T, Haseley D, Rogers J, Kinahan P. Clinical imaging characteristics of the positron emission mammography camera: PEM Flex Solo II. J Nucl Med. 2009;50:1666-75. doi:10.2967/jnumed.109.064345.
43. Gravel P, Surti S, Krishnamoorthy S, Karp JS, Matej S. Spatially-variant image-based modeling of PSF deformations with application to a limited angle geometry from a dual-panel breast-PET imager. Phys Med Biol. 2019;64:225015. doi:10.1088/1361-6560/ab4914.
44. Ravindranath B, Junnarkar S, Purschke ML, Maramraju S, Hong X, Tomasi D, et al. Results from prototype II of the BNL simultaneous PET-MRI dedicated breast scanner. 2009 IEEE Nuclear Science Symposium Conference Record (NSS/MIC): IEEE; 2009. p. 3315-7.

45. Tornai MP, Samanta S, Majewski S, Williams MB, Turkington TG, Register AZ, et al. High sensitivity dedicated dual-breast PET/MR imaging: concept and preliminary simulations. 15th International Workshop on Breast Imaging (IWBI2020): International Society for Optics and Photonics; 2020. p. 1151318.
46. Wang B, van Roosmalen J, Piët L, van Schie MA, Beekman FJ, Goorden MC. Voxelized ray-tracing simulation dedicated to multi-pinhole molecular breast tomosynthesis. Biomedical Physics & Engineering Express. 2017;3:045021.
47. Schulz V, Schug D, Gebhardt P, Gross-Weege N, Nolte T, Borgo M, et al. Improving the Diagnosis of Breast Cancer using a dedicated PET/MRI–The EU Project HYPMED. Nuklearmedizin. 2020;59:P43.

Figures

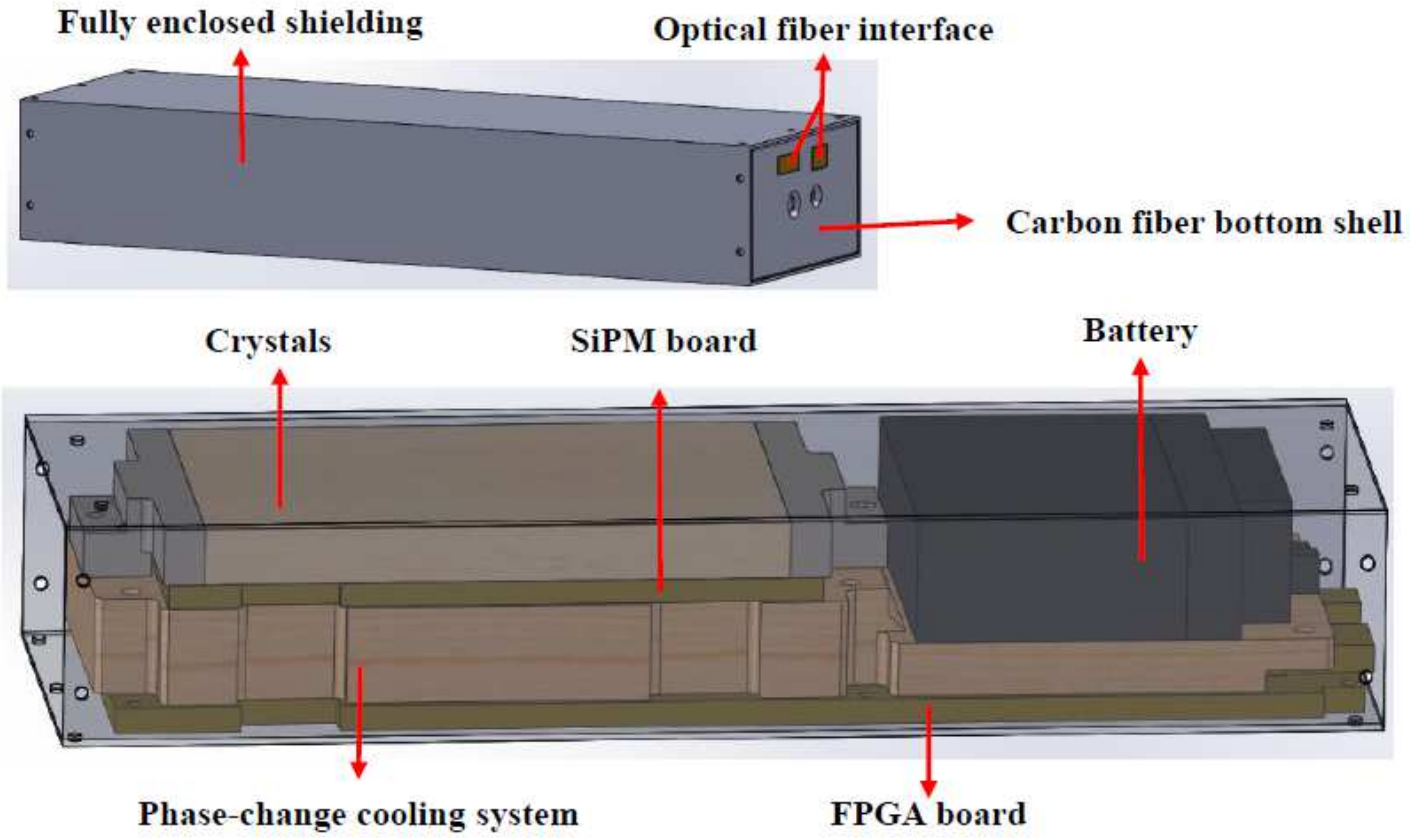

Figure 1

Mechanical structure of one detector module

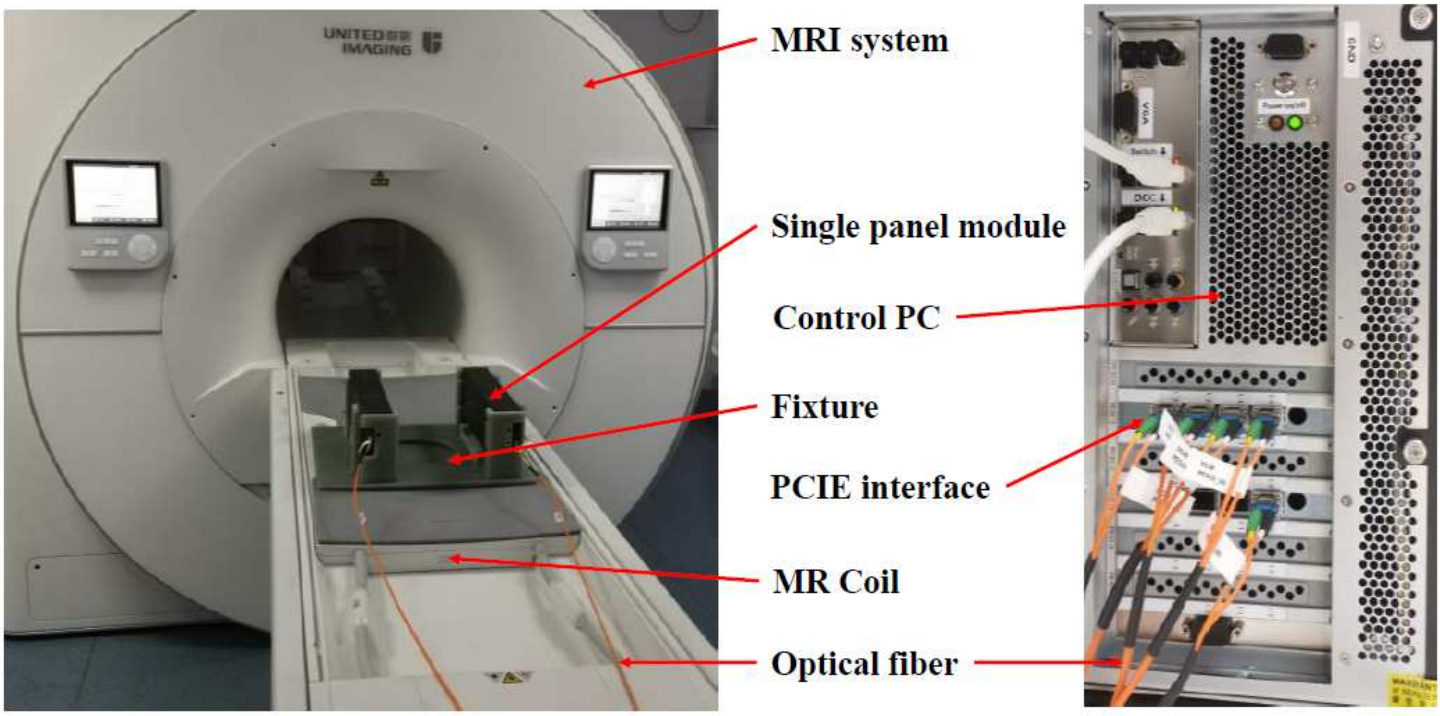

Figure 2

Picture of DP-PET inserted MR system

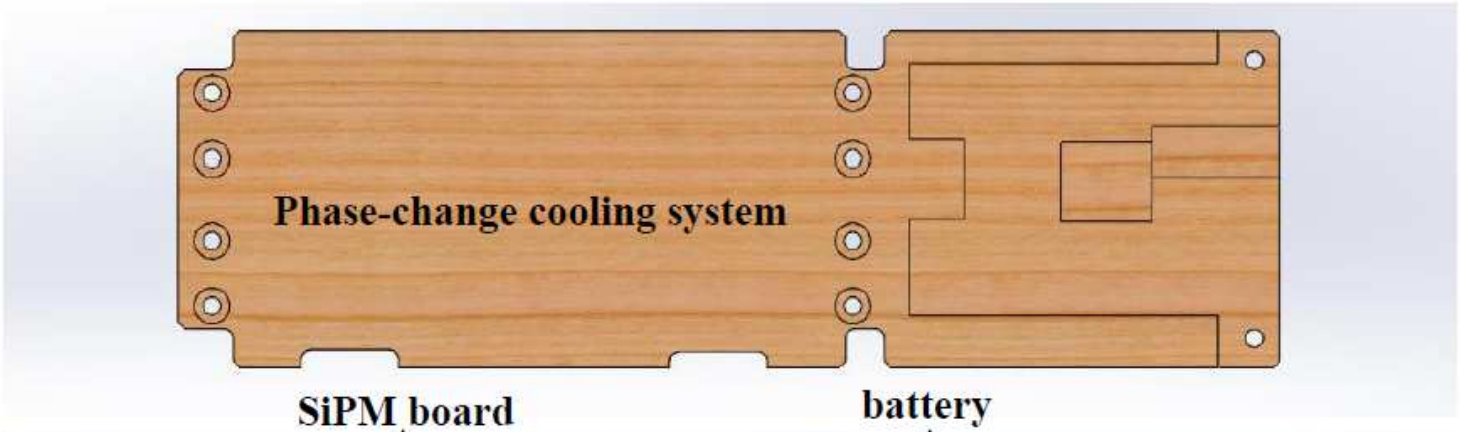

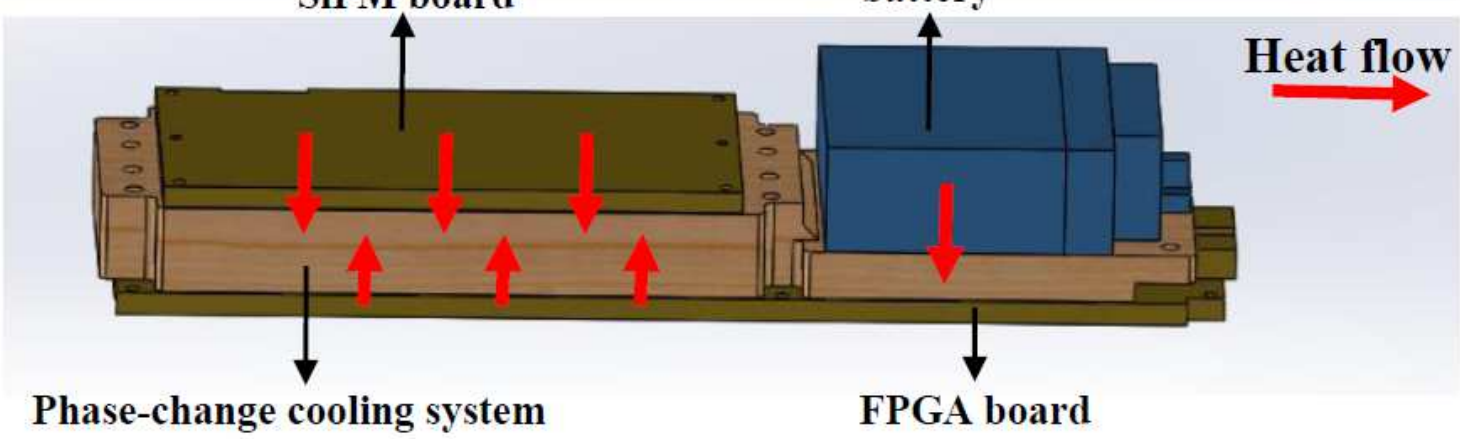

Figure 3

Schematic of phase-change cooling system

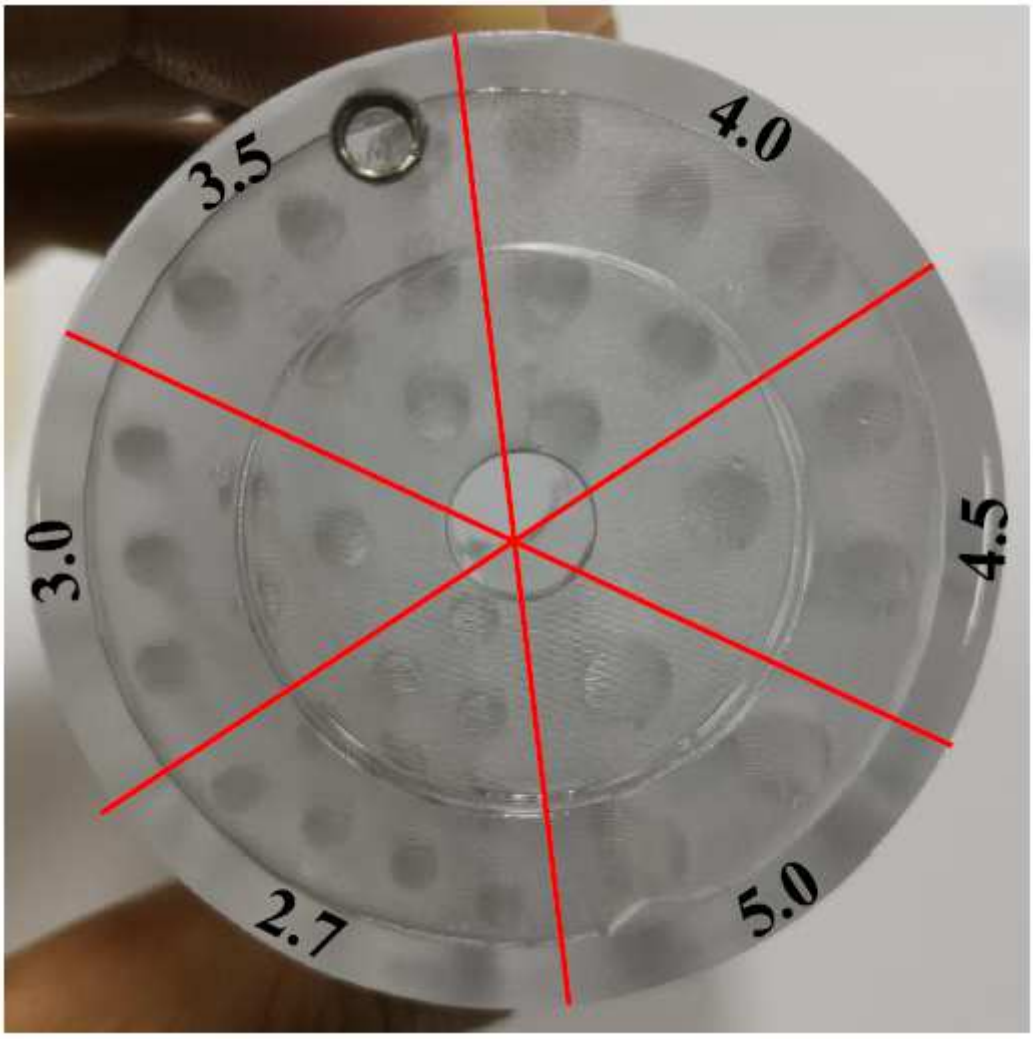

Figure 4

The Derenzo resolution phantom with rod diameters (in mm) indicated

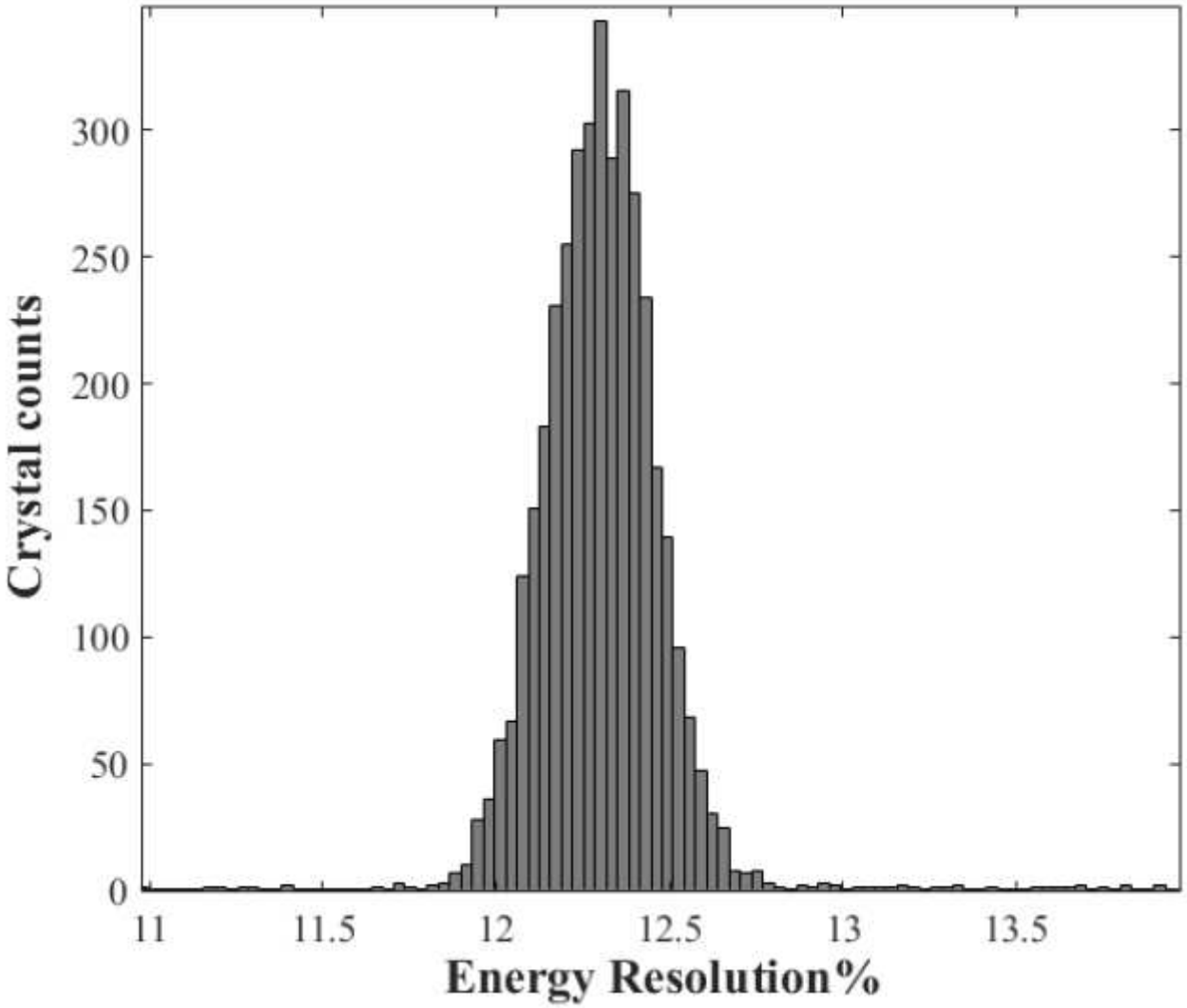

Figure 5

Energy resolution histogram of individual crystals

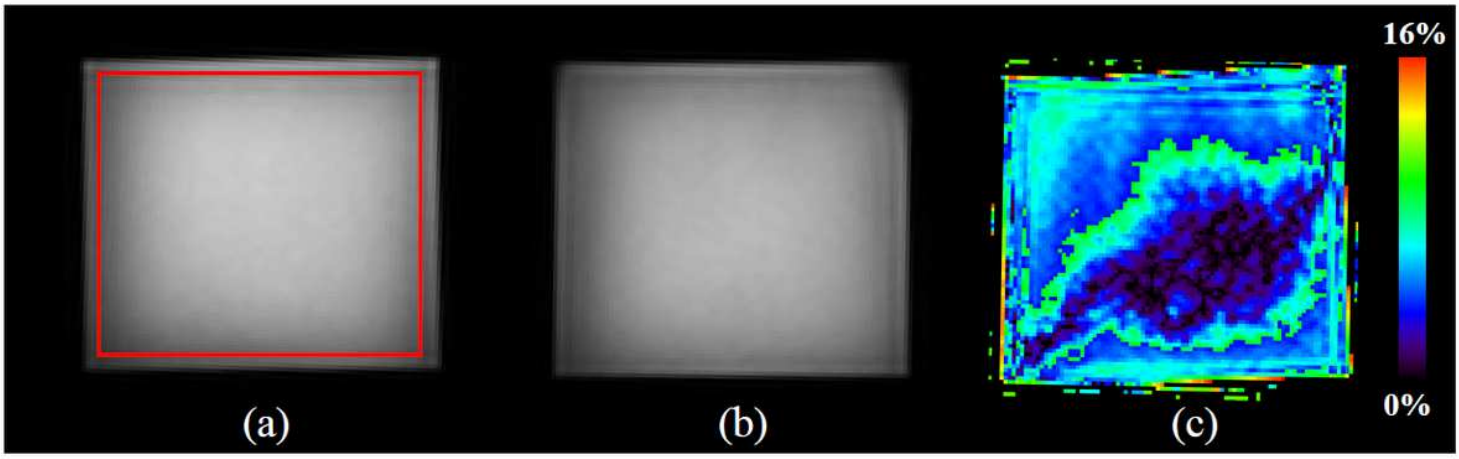

Figure 6

Dixon MR images with no DP-PET (a) and DP-PET inserted (b), and (c) is the result of subtracting (a) and (b)

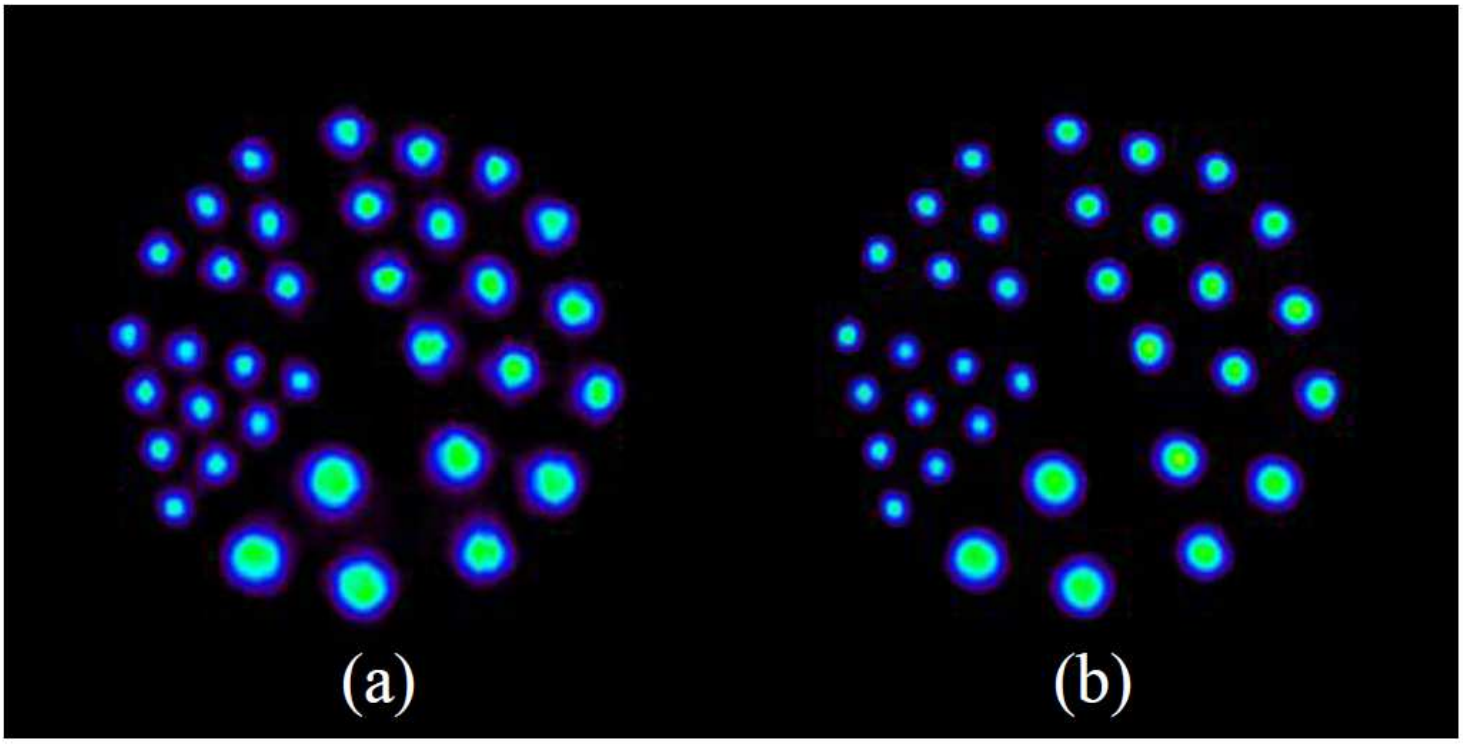

Figure 7

Images of the Derenzo phantom scanned parallel to the z direction with RM off (a) and RM on (b) from DP-PET scan